

Yaw Control of a Moving Axisymmetric Body using Synthetic Jets

Thomas J. Lambert^{*}, Bojan Vukasinovic[†] and Ari Glezer[‡]
Woodruff School of Mechanical Engineering,
Georgia Institute of Technology, Atlanta, GA 30332-0405

Synthetic jet actuators are utilized on a nominally 'free' yawing axisymmetric model to induce localized flow attachment over the body's aft end and thereby alter the dynamic model orientation. The model is supported by a vertical thin steel wire that passes through the model that undergoes natural oscillatory response to the oncoming flow. Hybrid fluidic actuation is effected using two independently driven aft-facing jet actuators that emanate from narrow, azimuthally-segmented slots, centered symmetrically on the opposite ends of the yawing plane, and placed on a circular tail end that extends into a Coanda surface. The body motion response is measured using a laser vibrometer, and the aft coupled body/flow dynamics is characterized using planar PIV. Continuous actuation schemes, independent of model motion, and the respective aerodynamic responses are investigated with 'open loop' fluidic control. In addition, a PID controller is developed to effect 'closed loop' fluidic control with optimally timed synthetic jet operation dependent on model motion. Fluidic actuation demonstrates up to 60% suppression of natural yaw oscillations, and can impose directional preference with open loop control. The closed loop control results in more prominent yaw oscillation suppression of about 90%, directional preference, or oscillation amplification, displaying a large potential for directional control authority of free flight aerodynamic bodies.

Nomenclature

A_j	actuator orifice cross-sectional area	t	time
c	model chord length	V_w	cross stream wake velocity
C_D, C_b, C_P	closed loop PID control coefficients	x	yawing axis downstream location
C_μ	jet momentum coefficient	U	streamwise velocity
C_1, C_2	closed loop jet scaling coefficients	U_0	free stream velocity
D	axisymmetric body diameter	U_j	maximum jet expulsion velocity
D_s	support wire diameter	ζ	planar vorticity
f	model oscillations frequency	θ	model yawing angle
f_c	characteristic frequency peak	θ_G	controller goal yawing angle
f_{con}	PID controller operation frequency	θ_{offset}	synthetic jet induced yaw offset
f_{res}	power spectra frequency resolution	θ_{P-P}	peak to peak angular displacement
f_s	model natural shedding frequency	θ_{RMS}	root mean square angular displacement
h_s	model backward-facing step height	τ_{conv}	model convective time scale
L_0	laser vibrometer downstream location	τ_{cycle}	synthetic jet cycle period
My	aerodynamic yawing moment	τ_{osc}	model oscillation cycle period
PSD	power spectral distribution	ω	model yaw angular velocity
R_c	Coanda surface radius	ω_G	controller goal yawing angular velocity

I. Technical Background

The present work considers manipulation of separated flows over external aerodynamic platforms and utilizes altered aerodynamic forces and moments that result from full or partial flow attachment to affect the platform orientation and trajectory. Previously, this has been typically accomplished using either actuation frequencies comparable with the platform's characteristic frequency (e.g., Hsiao et al.¹, Williams et al.², Chang et al.³, and Seifert et al.⁴) or at frequencies that are substantially higher (e.g., Erk⁵, Smith et al.⁶, 1998, Amitay et al.⁷, and Honohan et al.⁸). It has also been shown that more aggressive hybrid (combined active and passive) flow control

^{*} Graduate Research Assistant, AIAA Member.

[†] Research Engineer, AIAA Member.

[‡] Professor, Associate Fellow AIAA.

can be achieved by fluidic actuation over a Coanda surface, as shown in a substantial body of past work. As shown by Newman⁹, the flow direction of a planar jet can be substantially altered near the exit plane either by the jet adherence to a curved surface that is a smooth extension of the nozzle, or by the reattachment of a separated jet to an adjacent solid Coanda surface. Another passive flow modification that was considered in tandem with active flow control utilized a short rearward facing step to cause local flow separation¹⁰. This hybrid geometry has shown large potential for internal flow applications as well, such as controlling separation and adverse pressure gradients in a diffuser¹¹.

Hybrid flow control has also demonstrated significant potential applications to axisymmetric platforms with an objective of airborne flight dynamics control. Freund and Mungal¹² applied steady circumferentially-uniform blowing over Coanda surfaces at the aft corner of the body, leading to drag reduction up to 30%. Sigurdson¹³ considered the effect of using a sharp leading edge to induce flow separation and then controlling the flow through a slot at the leading edge of an axisymmetric body. Rinehart et al.^{14,15} investigated the generation of a normal force on an aerodynamic platform using the interaction of a single synthetic jet with an integrated axisymmetric Coanda surface. McMichael et al.¹⁶ were able to control the trajectory of a 40 mm axisymmetric spin stabilized projectile by exploiting separated base flow control which effected steering forces and moments. Abramson et al.¹⁷, investigated the effects of asymmetric flow actuation on an axisymmetric body of revolution with four, equally-spaced azimuthal synthetic jets issuing from within a rearward facing step in the tail, where the induced aerodynamic forces with fluidic actuation were found to have a saturation limit. Corke et al.¹⁸, reported the altered drag and side force, generated with a tangential blowing plasma actuator placed upstream of a Coanda surface on an axisymmetric body. Abramson et al.¹⁹ further studied different active control actuation schemes for possible utilization in steering and stabilizing an airborne axisymmetric body. Lambert et al.²⁰ studied the effect of active flow control schemes on an axisymmetric model with a controlled dynamic model orientation and found that the aerodynamic forces introduced by dynamic motion can be significantly suppressed or enhanced with appropriate timing and modulation of the active control.

An inherent problem with any experimental aerodynamic study of a nominally 'free' body is related to its mounting into a test section. Ideally, the model support should not cause aerodynamic interference (e.g., magnetic-force supports²¹), but the most predominant supports involve sting mounts that are directly in the body's wake. An alternative support, aimed at minimizing the wake-support interference, was utilized by Abramson et al.^{16,18} and Lambert et al.²⁰, where a model is supported by thin wires. Another inherent challenge in model support is that a nominally 'free' body also needs to be allowed a dynamic motion response within the realizable motions in a test section. For mechanical simplicity, a free pivot axis around a mounting wire was chosen to be implemented in the current system, such that the model could move freely in yaw and was constrained in other directions. In single-degree-of-freedom setups, the application of closed loop flow control is a relatively new development, with one such investigation done in 2006 on an airfoil through Kutay et al.²², where a similar conceptual closed loop approach is implemented in the present work on an axisymmetric body. The goal of the present experimental investigation is to assess the fundamental flow mechanisms that are associated with time-dependent flow control, and to characterize and control effected dynamic orientation changes due to hybrid flow control on a free moving axisymmetric platform in one degree of freedom.

II. Free Yawing Platform: Experimental Setup and Procedures

The investigation of yaw control of a single-degree-of-freedom axisymmetric body is conducted in the open-return wind tunnel at Georgia Tech having a test section that measures 91 cm on the side, with a test section speed, U_0 , of up to 40 m/s. The geometry of the wind tunnel model is the same as in the previous studies of the constrained-body configurations²⁰. Although the present model is also equipped with the azimuthal array of four independently-driven synthetic jet actuators that are equally distributed along the perimeter of the tail section, the aerodynamic control moments on the model are generated using the two actuators within the plane of the model yawing motion. Each jet is embedded into the surface having a $A_j = 0.38 \times 34.3$ mm rearward facing orifice that issues a jet over a Coanda surface formed by an azimuthal segment of an axisymmetric constant radius, $R_c = 12.7$ mm. The jet actuation leads to the partial attachment of the outer flow along the Coanda surface resulting in a reaction force by the turning of the outer flow into the wake region. The axisymmetric model is built using stereo-lithographed components and measures $D = 90$ mm in diameter and $c = 165$ mm in length. The entire model is hollow and designed to have minimum weight, consisting of a nose and a body piece that are held together with screws. A through hole is placed in the nose piece to allow mounting at a fixed location. The rear component with the Coanda surface has the cut-in grooves along the orifice edges that guide the jet flow and limit its span-wise

diffusion. The adjoining backward-facing step to the circumference of the body is $h_s = 1.5$ mm in height. The step height was chosen such that it is shallow enough to enable local flow attachment when the control jet is activated, but deep enough to prevent attachment of the free stream flow in the absence of the jet actuation.

All of the components used to mount this axisymmetric model in the wind tunnel are shown in Figure 1. The steel support wire, $D_s = 1$ mm, is selected to be thin enough to reduce the drag coefficient and decouple its vortex shedding from the model, while thick enough to minimize translational and rotational vibrations. The wire-mounting mechanism consists of two bearings, and a vented screw that is secured to a shaft connector (Figure 1a). The wire is held in place with the shaft connector, and is tightened by extending both vented screws from the tunnel wall. The model nose has two through holes that pass the support wire and the model is secured in place with two integrated shaft connectors from the inside. This yawing axis is chosen to be $x = 0.015c$ upstream of the center of pressure, such that the model is semi-stable. The rest of the model body containing the synthetic jet actuators is secured to the nose (Figure 1b). The electrical connection for the actuators is enabled by means of additional thin high voltage wires weaved along the support wire and through the tunnel walls, while the support wire provides the electrical ground. The experimental model supported inside of the test section is shown in Figure 1c.

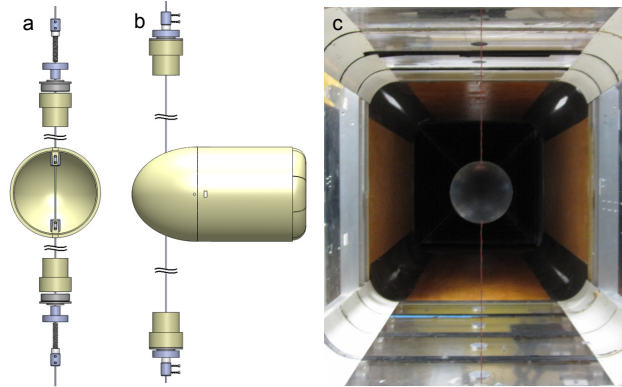


Figure 1. Unassembled (a) and assembled (b) $D = 90$ mm axisymmetric CAD model and mounting mechanism, and upstream view of the model mounted in the tunnel (c).

Measurement of the model angle is acquired by the means of a laser vibrometer sensor mounted normal to the side wall of the test section at a fixed distance L_0 downstream of the model mounting wire. The vibrometer measures the velocity of the surface normal to the laser as an analog signal, and uses a built in low pass integrator to create a second analog signal of the position of the surface. Two surface positions and velocities are needed for a transformation into the model angular position and velocity, so a fixed mounting axis is assumed. The angle, θ , is then extracted from the laser vibrometer measured signal, distance L_0 , and the model diameter, D . The wake is characterized in the model central yawing plane by the PIV measurements. A horizontal PIV laser sheet is steered from the opposite tunnel side as the vibrometer, where the model blocks the laser light from affecting the vibrometer measurements. The PIV camera is mounted on top of the test section, having a capability for traversing in both the streamwise and cross-stream directions.

III. Baseline Response of the Free Yawing Platform

A primary objective of the present work is to assess the efficacy of synthetic jet flow control in the presence of a dynamically-changing aerodynamic environment. In order to characterize this efficacy, the baseline flow is first characterized in more detail. The model's response is constrained by the mounting mechanism described in Section II to respond only in one degree of freedom (yaw), where every care was taken to minimize yaw friction. The mounted model is semi-stable: initial perturbations cause the model to oscillate when the model is exposed to flow. The self-excited oscillations are attributed to the lag between the model's dynamic wake response and its instantaneous orientations, as discussed in conjunction with Figure 4. An illustration for such a model oscillation is shown in Figure 2 at $U_0 = 20$ m/s. Figure 2a shows a time trace of the model angular position normalized by convective time scales ($\tau_{conv} = c/U_0 = 8.25$ ms), while the

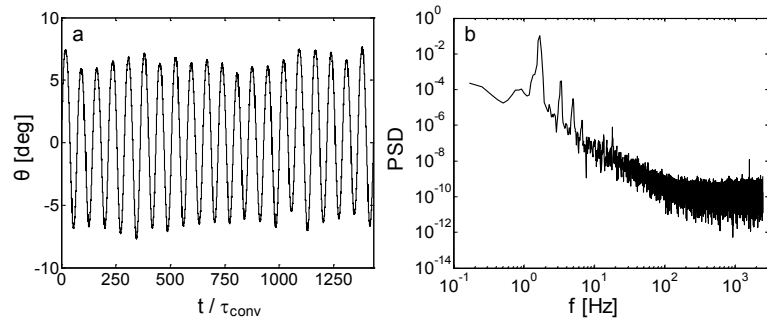


Figure 2: A time-trace of the baseline model oscillation ($U_0 = 20$ m/s) measured by the laser vibrometer (a) and the corresponding power spectra (b) of displacement fluctuations.

corresponding power spectrum is shown in Figure 2b. The power spectrum was based on twenty cycles of the baseline motion which yielded a frequency resolution of $f_{res} = 0.08$ Hz, and shows a characteristic frequency peak at $f_c \approx 1.7$ Hz, along with its higher harmonics. The value of f_c , as well as the RMS amplitude of oscillation, θ_{RMS} , varies with U_0 and the variation of both of these parameters is shown in Figure 3. Figure 3a shows the variation of f_c with U_0 which has a strong linear effect. It should be noted, however, that f_c is more than an order of magnitude lower than the natural shedding frequency, f_s , from the axisymmetric body under the present conditions. Figure 3b shows the complete cycle RMS for ≈ 100 s (rounded down to an integer number of oscillation periods from the start time), and shows proportionality to U_0 between 14 m/s and 36 m/s, with a deviation in slope for very high and very low U_0 . It is noted that the RMS angle exhibits a weak saturation effect with higher U_0 .

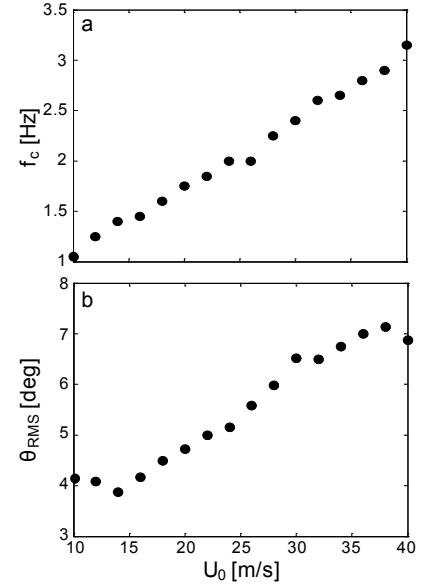


Figure 3: Baseline variation of primary model oscillation frequency, f_c (a), and RMS amplitude, θ_{RMS} (b) with variable free stream speed, U_0 .

A series of PIV measurements was taken conditionally averaged relative to the baseline oscillation cycle of the model. For each of the phases of that cycle, 170 image pairs are taken and averaged, with triggering off the vibrometer-measured model orientations. Figure 4 presents such phase-averaged wake flow fields for one half of the cycle overlaid upon contours of the in-plane vorticity, ζ . The angular convention utilized is that the yawing angle and angular velocity, θ and ω , are positive in the counter clockwise direction. The phases presented are $\theta = 0^\circ, -2^\circ, -4^\circ$, and -6° , shown with negative angular velocity, ω , in Figure 4a-d, and positive ω in Figure 4e-h, with a $\theta_{RMS} \approx 5^\circ$. It is interesting to note that the cross-stream velocity of particles in the wake, V_w , lag compared to ω . In Figure 4a, V_w is slightly positive (with a positive convention to the left) when ω is heavily negative, while, in Figure 4d, V_w is strongly negative when ω is small, and, in Figure 4e, V_w is slightly negative when ω is strongly positive. This suggests that the reaction force the wake effects on the model is out of phase with the position of the model, and is in accord with assumption that the initial baseline oscillation is caused by aerodynamic instability due to such a phase lag. Another interesting note is that ζ in the shear layer depends primarily on θ , while depending very weakly on ω (compare Figure 4a-d to Figure 4e-h).

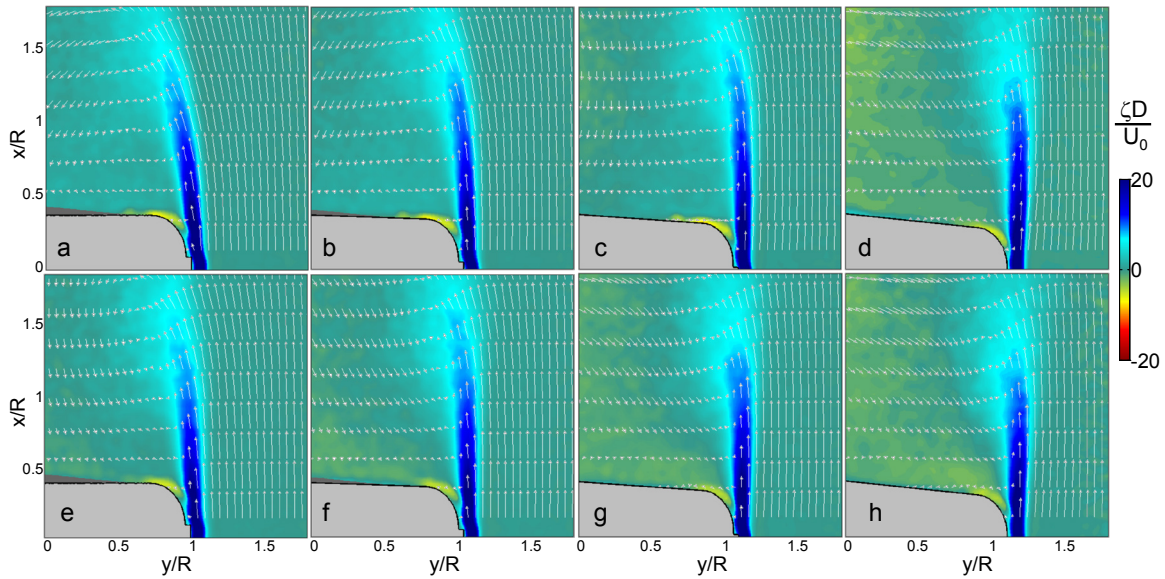


Figure 4: Raster plots of the in-plane vorticity, ζ , with overlaid velocity field of the baseline flow ($U_0 = 20$ m/s) averaged at model's deflections $\theta = 0^\circ$ (a,e), -2° (b,f), -4° (c,g), and -6° (d,h), with negative (a-d) and positive (e-h) angular velocities, ω .

IV. Free Yawing Platform Response to Continuous Actuation

There are two flow control schemes that are utilized in the present work, the first being a continuous actuation of jets regardless of the model dynamic position in the cycle, and the second being a dynamic actuation and termination of the jet actuation with respect to the model's dynamic position. The benefit of continuous, 'open loop' actuation is in simplicity of its implementation for a free-flight body, while the benefit of dynamic actuation is the ability to take advantage of transient effects of the flow attachment, as well as to adjust control input based on the altered aerodynamic forces and moments coupled to body response due to the initial jet actuation, leading to a more substantial change in the body motion. The off-resonance frequency of operation is chosen such that the maximum expulsion velocity, $U_j \approx 25$ m/s, is obtained for each synthetic jet, yielding a jet cycle period of $\tau_{cycle} = 625$ μ s.

Initially, the effect of continuous actuation is examined at $U_0 = 20$ m/s with two different control schemes: a single-jet and both-jets control, along with the unactuated (baseline) flow. Instantaneous measurements of all three of these scenarios are shown in Figure 5, with the operational jet momentum coefficient, $C_\mu = (U_j^2 \cdot A_j) / (U_0^2 \cdot \pi D^2) = 0.003$. The data are taken over sampling intervals of 2400 convective time scales where actuation is activated at $t = 600 \tau_{conv}$ and is terminated at $t = 1800 \tau_{conv}$ from the starting point. Figure 5a shows the instantaneous baseline behavior of the model oscillation, and it is observed that while the frequency is well behaved, the nominal oscillation amplitude is modulated. When the flow is unactuated, the model oscillates around 0° , where it is aligned with the free stream. When the flow is actuated by the right actuator (Figure 5b), the model rotates counter clockwise around the support axis and oscillates about $\theta = 3.5^\circ$, and a similar effect opposite in direction occurs when the left actuator is activated. It is noted that the left and right actuation effects occur at a faster rate than one oscillation cycle ($\tau_{osc} = .588$ s), where the maximum change from the continuous actuation occurs during the first oscillation cycle. Figure 5c shows when both jets are activated the model remains centered about zero degrees, similar to the baseline case. However, the oscillation amplitude decreases from 7° to about 2.5° , causing roughly a 60 percent suppression in baseline oscillation amplitude. It is also noteworthy that this decrease with both jets activated does not occur as fast as the offset deflection in the single jet activation case, where the suppression in cycle oscillation amplitude occurs between $5-6 \tau_{osc}$.

The single jet open loop control from Figure 5b is investigated in more detail with the average of 25 data sets in Figure 6 with phase plots of ω vs. θ in Figures 6a and b, and the yaw moment, M_y vs. θ , in Figures 6c and d, where M_y was calculated using a numerical derivative of ω along with the model's rotational inertia. Figures 6a and c show the transient onset of a single jet from $120 \tau_{conv}$ before to $600 \tau_{conv}$ afterwards, with actuation segment shown in blue. Similarly, Figures 6b and d show the transient termination of the single jet continuous actuation from $120 \tau_{conv}$ before to $600 \tau_{conv}$ afterwards. Initially, the baseline flow has an elliptical path in ω vs. θ , which is to be expected from quasi-sinusoidal motion, where the angular velocity would lag the position. Figure 6a shows when actuation is applied, the model vibration becomes deflected to higher angles within one τ_{osc} , but the oscillation occurs with a diminished range of positions and velocities, where the baseline oscillation range was $\pm 7^\circ$ and $\pm 75^\circ/s$ and it is diminished to $\pm 6^\circ$ and $\pm 60^\circ/s$ with a new oscillation center of $\theta = 3.5^\circ$. The termination of actuation is shown in Figure 6b, where the oscillation returns to baseline within one τ_{osc} . There are two notable moment peaks that emerge in the M_y vs. θ plots in Figures 6c and d that occur after the model has reached its peak angle and reversed direction, which may be attributed to a reaction moment of vortex separation off of the wake of the model where the wake had the tendency to continue in the same direction the model was previously moving. When actuation is applied in Figure 6c, the range of the yaw moment is also diminished from ± 0.18 Nm to ± 0.16 Nm, similar to the angular velocity. In addition, the vortex shedding peak that occurs at the $-\theta$ disappears while the peak at the $+\theta$ becomes enhanced, which is commensurate with the modified model

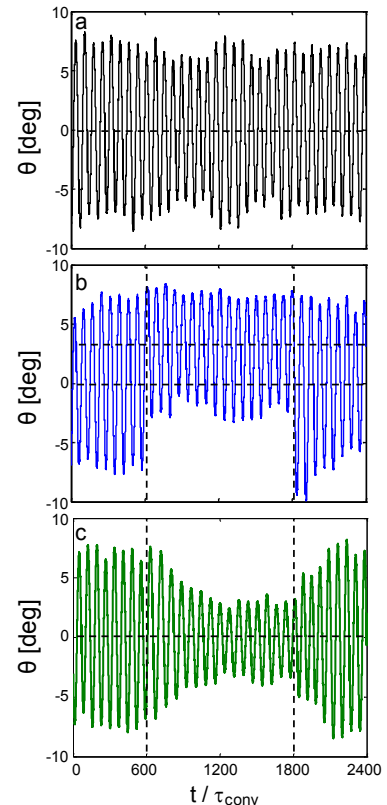


Figure 5: Instantaneous variation of the model deflection angle, θ , for baseline (a), and actuated flows with single jet (b), and both jets (c) at $U_0 = 20$ m/s and $C_\mu = 0.003$.

motion traveling through a small $-\theta$ to a large $+\theta$. The effect of actuation termination on the model moment is shown in Figure 6d, where the model oscillation returns to center with a range similar to the initial baseline motion (compare Figures 6c and d), with the exception that the baseline peaks have not yet reemerged after $600\tau_{conv}$.

A closer study of the suppression of model vibration in Figure 5c is shown in Figure 7 with phase plots analogous to Figure 6, with ω vs. θ in Figures 7a and b, and M_y vs. θ in Figures 7c and d. Figures 7a and c show the transient onset of both jets from $120\tau_{conv}$ before to $600\tau_{conv}$ afterwards, while Figures 7b and d show the transient termination of both jets from $120\tau_{conv}$ before to $600\tau_{conv}$ afterwards, with actuation segment shown in green. The baseline flow of Figure 7, shown in black, is analogous to the baseline flow present in Figure 6, with an ellipsoidal path in angular velocity and with moment peaks emerged at the extremes of the motion. Upon the onset of actuation the model vibration slowly reduces over several cycles in Figure 7a, with the oscillation reducing to a value of $\pm 2.5^\circ$ and $\pm 30^\circ/s$, while upon termination the model vibration slowly returns to baseline in Figure 7b. Upon actuation, Figure 7c, the model moment path diminishes from ± 0.18 Nm to ± 0.05 Nm, but its path resembles the initial baseline path including the peaks until a few oscillation cycles have passed, and then finally collapses into an ellipsoidal path. The absence of the moment peaks in the model path with both jets actuation is in agreement with the absence of the peak in the single jet actuation $-\theta$, where the moment peak only occurs when the model moves to a large enough angle. This shows that the actuated motion of the model is more stable at smaller excursions, where large aerodynamic moments are induced at a faster rate when the model is yawed further from center. Upon termination, the model returns to the baseline moment curve, but the path remains elliptical, and the

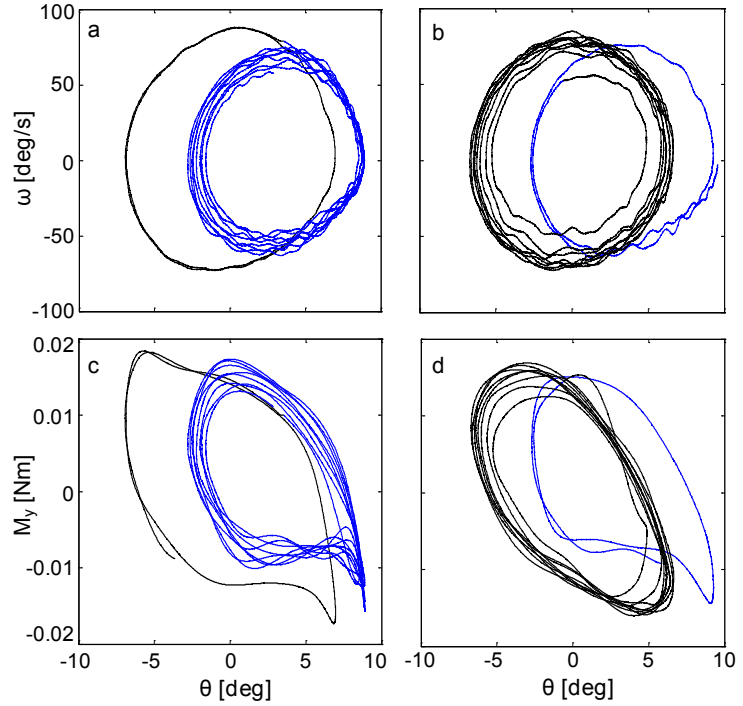


Figure 6: Phase plot of 25 averages of angular velocity, ω (a,b), and yaw moment, M_y (c,d) for $120\tau_{conv}$ prior to $600\tau_{conv}$ after the transient activation (a,c), and termination (b,d) of single jet continuous actuation at $U_0 = 20$ m/s and $C_\mu = 0.003$.

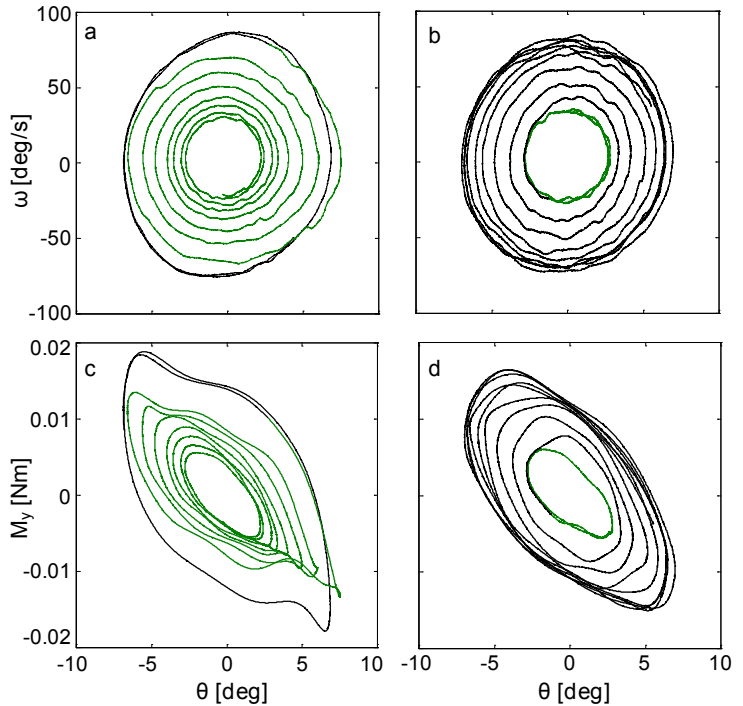


Figure 7: Phase plot of 25 averages of angular velocity, ω (a,b), and yaw moment, M_y (c,d) for $120\tau_{conv}$ prior to $600\tau_{conv}$ after the transient activation (a,c), and termination (b,d) of both jets continuous actuation at $U_0 = 20$ m/s and $C_\mu = 0.003$.

peaks have yet to reemerge, even after the passage of $600\tau_{conv}$.

The same study shown in Figures 6 and 7 were conducted over a wide range of U_0 and the results are presented in terms of the average steady state deflection of the model with one jet continuously actuated, and the average steady state model oscillation reduction, shown respectively in Figures 8a and 8b. In Figure 8a, the model deflection, θ_{offset} , is normalized by the peak to peak amplitude of the baseline vibration, θ_{p-p} , and this deflection seems to have a saturation effect of 30%, at $U_0 \geq 20$ m/s, with smaller deflection at $U_0 < 20$ m/s. In Figure

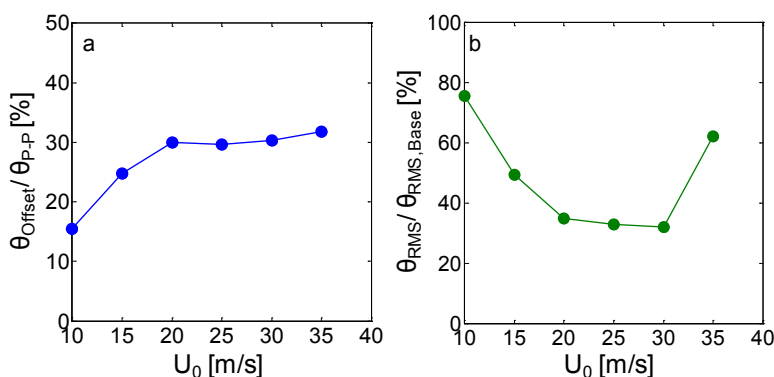


Figure 8: Induced average deflection percentage with single jet actuation (a), and oscillation suppression percentage with both jets actuation (b) with variable free stream speed, U_0 , at $C_\mu = 0.003$.

8b, the reduced θ_{RMS} is normalized by θ_{RMS} of the baseline and a similar phenomenon is observed where there is a build up on vibration reduction percentage from 10 to 20 m/s and then saturation from 20 to 30 m/s at 40%, with a decrease in vibration reduction at 35 m/s, presumably caused from the limiting jet momentum at this speed.

Figure 9 presents the effect of continuous actuation on the time scale of the model oscillation, where the initial $\theta = 4^\circ$, with a positive initial ω . The time steps are chosen to be $125\tau_{cycle}$, $250\tau_{cycle}$, and $375\tau_{cycle}$ (~85 ms, ~169ms, and ~253ms, respectively), and the average θ that the model attains at the corresponding times is shown below each frame. Figures 9a-d depicts the baseline motion of the model in these time steps. Initially, the model reaches close to its full displacement in Figure 9b, reverses velocity and starts moving back to center in Figure 9c, and crosses past zero in Figure 9d. The effect of continuously actuating the flow for this time duration is shown in Figure 9e-h, where the model position is initially unchanged relative to the baseline (Figure 9e) at the onset of actuation. Once the control jet is activated, comparison between Figures 9b-d to 9f-h shows the wake being vectored towards the model, causing a reaction moment towards negative θ . Initially the model position is least effected in the first time step, and most effected in the final time step, where the effect of the wake vectoring becomes stronger when the jet is inclined into the direction of flow, in agreement with previous study by Lambert et al.²⁰.

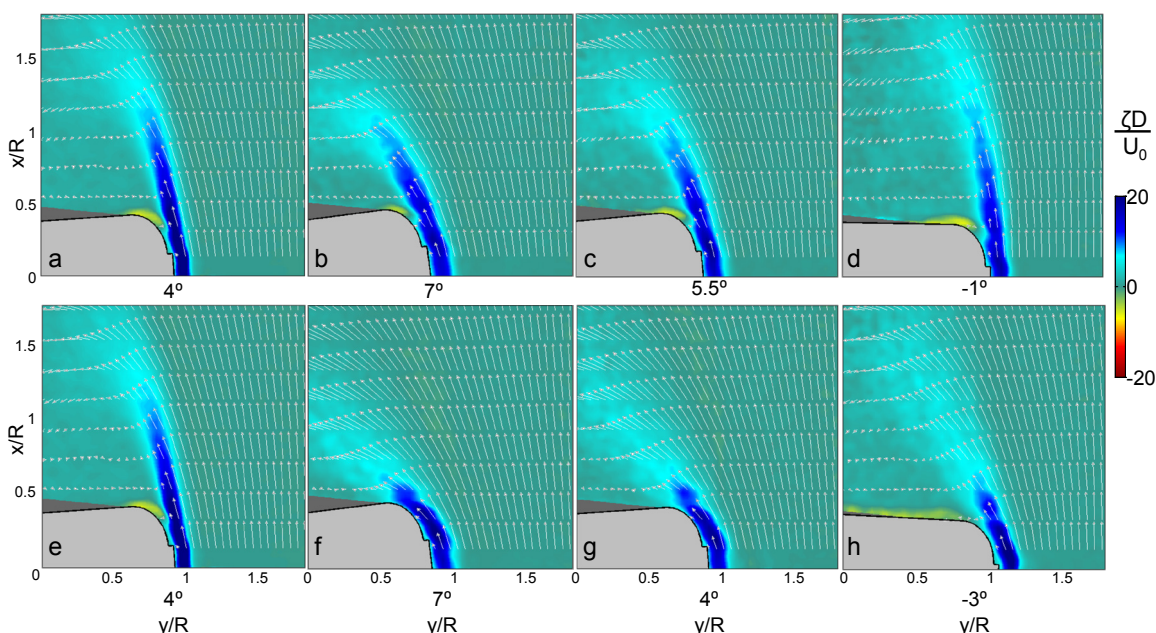


Figure 9: Raster plots of the in-plane vorticity, ζ , with overlaid velocity field of the baseline flow ($U_0 = 20$ m/s) with an initial model deflection of $\theta = 4^\circ$, at $t/\tau_{cycle} = 0$ (a,e), 125 (b,f), 250 (c,g), and 375 (d,h) after actuation onset for the baseline (a-d), and in-plane jet actuation at $C_\mu = 0.003$ (e-h). The corresponding model deflections are marked below each frame.

V. Effects of Transitory Actuation on the Free Yawing Platform

Before investigating the body-coupled dynamics of activation and termination of the jet control, an investigation of the transient activation of the synthetic jets is conducted to analyze the mechanisms of the localized flow vectoring and attachment on a free moving body of revolution. The analogous comparison of fluidic flow attachment to a *fully constrained* body of revolution was investigated by Rinehart^{14,15}, and is used for comparison. Two cases of interest are presented with the body (and synthetic jet orifice) declined away from free stream, $\theta = 3^\circ$ (Figure 10), and inclined into free stream, $\theta = -3^\circ$ (Figure 11), both with ω such that the model is moving away from center. Both of these cases are characterized with the mean phase-locked vector fields when the initial model angular velocities are oriented away from center. Both figures capture the very onset of the actuation, which is represented by six time steps after the actuation onset, at $t/\tau_{cycle} = 0, 4, 8, 12, 16,$ and 20 .

Figure 10a shows the baseline flow state at the onset of actuation: dominant vorticity is concentrated in the separating boundary layer coupled to the evolving shear layer that bounds the model wake. The flow clearly separates off the short backward-facing step above the jet orifice, and a strong signature of the opposing flow along the model surface is marked by the opposite-sense vorticity. Figure 10b shows the flow captured at a moment when four jet-actuation cycles are completed. The large starting vortex is fully formed downstream from the body, as it entrains the outer flow and the wake grows in size. At the same time, under the action of the small-scale (unresolved in this view) jet vortices, the flow immediately near the body surface is vectored along the Coanda surface that extends downstream from the jet orifice. At the next instant in time (Figure 10c), the starting vortex is already shed into the wake, which disconnects the shear layer vorticity sheet. The re-growing shear layer curls into the wake, and the outer flow begins to vector into the wake not only along the model surface (small-scale effect), but also along the trail of the starting vortex. By the full twelve actuation cycles (Figure 10d), a clear vectored shear layer is formed, which is also accompanied by its widening, i.e., an increase in its characteristic scale from Figure 10c. After 16 actuation cycles, the wake is fully vectored (Figure 10e), and only minor differences in the wake structure can be noted over a long time span (compare Figures 10e and f). The overall time scale on which the full actuation effect is established is in good agreement with previous work on the constrained model¹⁵, where the full vectoring effect was found to be established after about one convective time scale. The present work on the unconstrained model indicates somewhat longer time scale, but still less than one and a half of the convective time scale ($20\tau_{cycle} \approx 1.3\tau_{conv}$).

Figure 11 shows the analogous flow evolution to that of Figure 10, with a mirroring of θ around the centerline, and an opposite sense of ω . The development of the flow vectoring occurs in a similar fashion to that of Figure 10, with some important differences. First, in Figure 11a the shear layer is initially 'stronger', extending to a larger downstream location (compare Figure 10a to 11a), where the initial vorticity layer size is dependent on θ , and weakly on ω , as shown previously in Figure 4. Secondly, the growth and detachment of the starting vortex, shown in Figure 11b and 11c, is larger when the backward facing step is inclined into the free

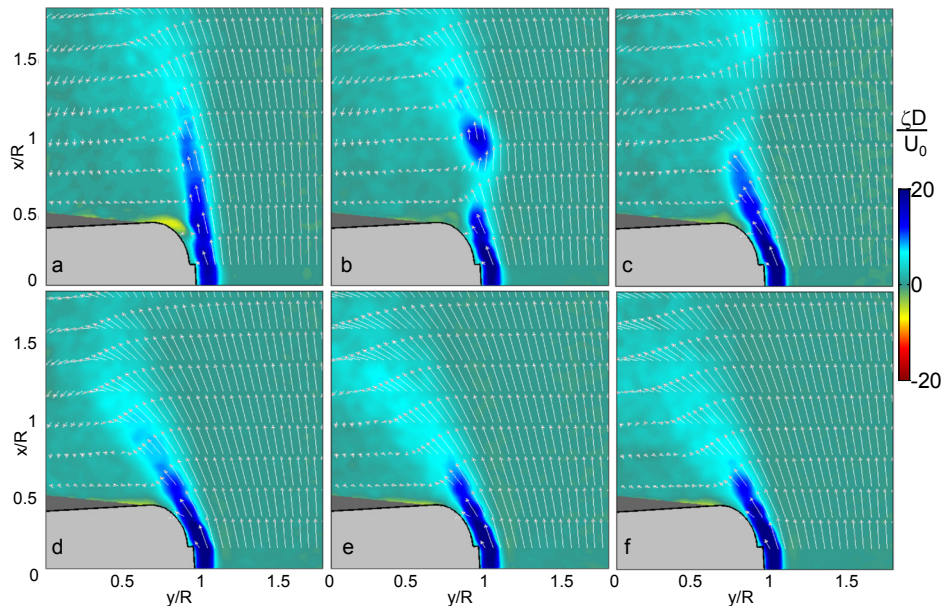


Figure 10: Raster plots of the in-plane vorticity, ζ , with overlaid velocity field of the transient onset of synthetic jet actuation ($U_0 = 20$ m/s and $C_\mu = 0.003$) at initial model's deflection $\theta = 3^\circ$, with positive ω , phase locked at $t/\tau_{cycle} = 0$ (a), 4 (b), 8 (c), 12 (d), 16 (e), and 20 (f).

stream, where the characteristic scale of this starting vortex is similar to the scale of the initial baseline shear layer. This result is in accord with the findings in the case of a stationary body that the change in force relative to the baseline state by the control jet is greater when the model is inclined into the free stream²⁰. Similar to the deflection towards the wake (Figure 10), it is seen that the full vectoring effect is attained after about sixteen actuation cycles (Figure 11e), and the somewhat weaker vectoring observed in Figure 11f is attributed to the continuing model deflection into the free stream from sixteen to twenty actuation periods between Figures 11e and 11f.

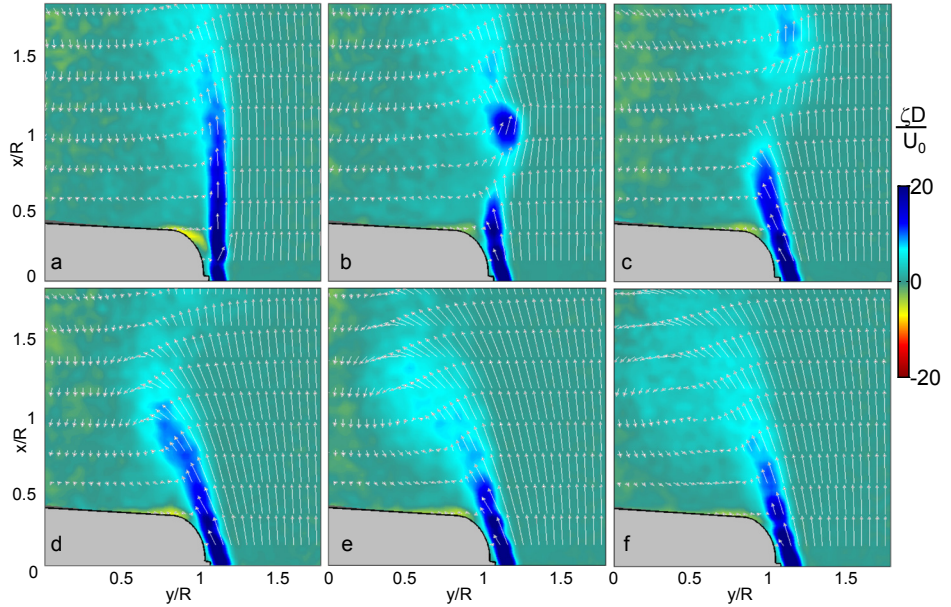


Figure 11: Raster plots of the in-plane vorticity, ζ , with overlaid velocity field of the transient onset of synthetic jet actuation ($U_0 = 20$ m/s and $C_\mu = 0.003$) at initial model's deflection $\theta = -3^\circ$, with negative ω , phase locked at $t/\tau_{cycle} = 0$ (a), 4 (b), 8 (c), 12 (d), 16 (e), and 20 (f).

As the analysis of Figures 10 and 11 indicates significance of a *combined* effect of both the small-scale actuation vortices and a large-scale starting vortex, further insight into their relative significance is sought by activation of packets of high-frequency actuation cycles, each of τ_{cycle} period, in a burst mode. Each of such packets of actuation is inherently associated with a single large-scale starting vortex. This study utilizes the same two model states investigated in Figures 10 and 11, with initial orientations of $\theta = 3^\circ$, and positive ω shown in Figure 12a, and $\theta = -3^\circ$, and negative ω shown in Figure 12b. As the model assumes each of these orientations during its natural oscillations, the burst actuation pattern is applied that consists of 1, 5, 10, 50, or 100 actuation cycles. The model's response to these actuation patterns is recorded by the vibrometer, and model is allowed afterwards to return to its baseline state. This sequence is repeated fifty times for each of the burst cycles, and the averaged model trajectories are shown in Figure 12, along with the baseline model trajectory over a single oscillation period, beginning at the onset of actuation ($t = 0$). In both Figures 12a and 12b, the effect of actuation on the baseline model motion appears to monotonically increase with the number of pulses, right from the onset of actuation. In Figure 12a, the initial orientation of the model causes the jet pulses to suppress the model oscillation, and as the model oscillation is suppressed, the period of the model oscillation is also decreased monotonically with the extent of the burst duration. It should be noted that there is virtually no effect of the single-pulse burst, when a single starting vortex is accompanied by only a single small-scale vortex,

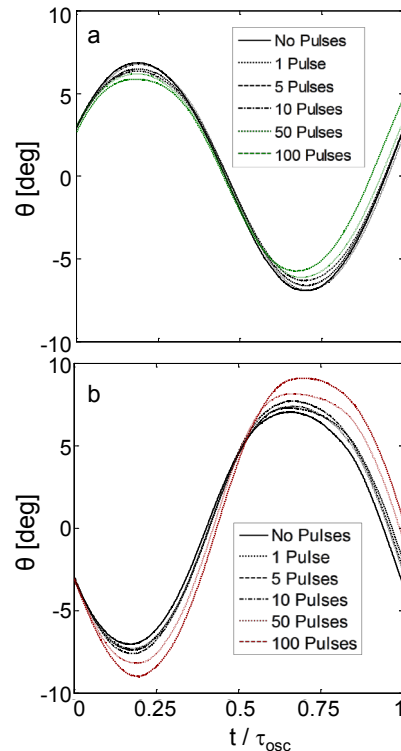


Figure 12: Phase-averaged transient response of the model position with a width of the burst actuation cycle (number of actuation periods) for initial $\theta = 3^\circ$ (a) and -3° (b), at $U_0 = 20$ m/s and $C_\mu = 0.003$.

and this finding stresses the importance of the small-scale actuation on the external flow vectoring. As the model orientation is mirrored in Figure 12b, the actuation effectively amplifies the model natural oscillations. Similar to the trends seen in Figure 12a, amplification in model displacement increases with the burst period, which also leads to monotonic increase in the oscillation period. Furthermore, a sole existence of the starting vortex is not sufficient to impose alterations to the model trajectory, but it is successive train of small-scale vortices that plays a dominant role in the induced effect.

The effect of the number of actuation pulses on the wake development is further characterized by the phase-averaged PIV of 170 individual measurements, which are shown in Figure 13. The initial orientation of the model is the same as Figure 12b, with $\theta = -3^\circ$, and negative ω , and this initial orientation is shown in Figures 13a,e, and i. The phase-averaged measurements are taken at $t/\tau_{cycle} = 0, 5, 10,$ and 15 from the initial orientation. Figures 13a-d show the unactuated wake variation due to the model motion over fifteen actuation cycles, which is only about 0.5° in model deflection. Such a small model deflection results in negligible difference among the flow fields in Figures 13a-d. The flow fields under the single-cycle burst actuation are shown in Figures 13e-h at equivalent time instances. Note that the corresponding model trajectory is shown in Figure 12b. Clearly, at the onset of actuation (Figure 13e), the flow field does not differ from the baseline, but after the five actuation periods (Figure 13f), the large-scale starting vortex is already fully formed and shed. Note that there is no significant vectoring of the flow along Coanda surface at the tail. By the ten actuation periods (Figure 13g), the recoiling severed shear layer entrains some of the fluid into the wake, further away from the body, while there is no flow vectoring along the body surface. As the time progresses (Figure 13h), the initial shear layer is re-established back to the baseline, while the large-scale vortex rolls into the wake away from the body. As a consequence, there is no immediate flow vectoring over the body surface at any instant in time. Figures 13i-l show the flow response to continuous jet actuation, as opposed to the single-period (“pulse”) actuation shown in Figures 13e-h. It is interesting to note that the global flow field is very similar after five actuation periods (compare Figures 13j and f): the effect of the large-scale starting vortex

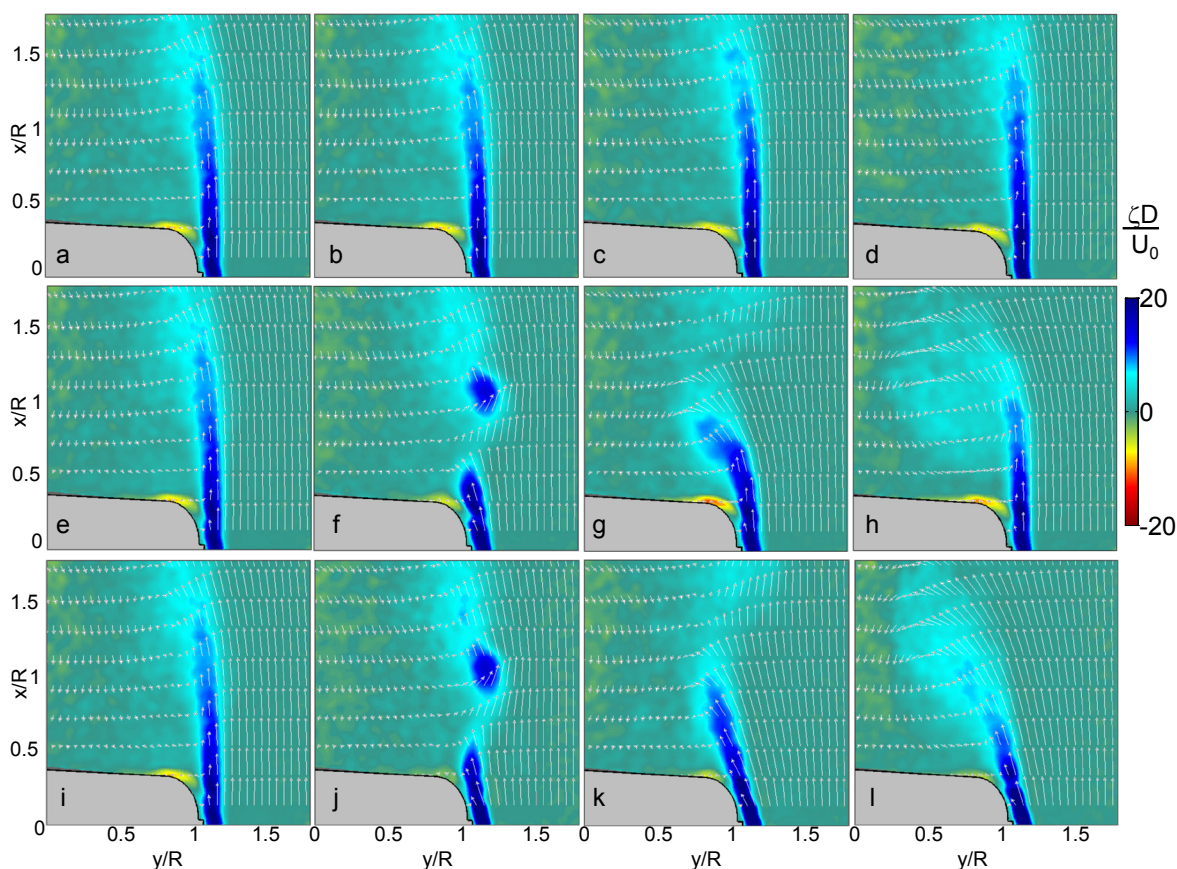


Figure 13: Raster plots of the in-plane vorticity, ζ , with overlaid velocity field of the transient onset of synthetic jet control ($U_0 = 20$ m/s and $C_\mu = 0.003$) at model's deflection $\theta = -3^\circ$, phase locked at $t/\tau_{cycle} = 0$ (a,e,i), 5 (b,f,j), 10 (c,g,k), and 15 (d,h,l), for the baseline flow (a-d), a single-pulse (e-h), and continuous (i-l) control.

should be invariant in these two cases, as expected. However, the major difference can be seen near the body surface: during the continuous actuation, there is a notable flow vectoring along Coanda surface, which is a signature of the near-field vectoring effect. Furthermore, as the shear layer recoils (Figure 13k), it is associated with a strong outer flow vectoring over Coanda surface, which is absent from the single-period actuation (Figure 13g). Finally, after the fifteen actuation periods (Figure 13l) there is the most dramatic difference in the wake alteration when compared with the single-period actuation, as the full wake vectoring is achieved. Therefore, the pre-selected actuation scheme for the closed-loop control approach is set to utilize continuous cycles, where successive actuation cycles are applied continuously, rather than with single-period cycles.

VI. Development of a PID Controller

In Section IV, the open-loop activation of the synthetic jets is shown to significantly alter the model's yawing angle. However, this open-loop approach does not take advantage of optimal activation duration by individual jets²⁰, and it is argued that utilization of a closed-loop control is necessary for an optimal response path. Therefore, the final step of the present investigation is the development of a closed loop controller to control the model's yawing angle. To illustrate this approach, a PID controller is developed, which utilizes a laser vibrometer as the sensor of the model's angular displacement, θ . The general theory of a PID controller uses the difference in the goal output, θ_G , from the sensor output, θ , as the proportional error (σ_P), and then uses a numerical integral and numerical derivative of σ_P to obtain the integral error (σ_I) and derivative error (σ_D), respectively. A command signal is created as a weighted superposition of all three of these using respective coefficients (C_P , C_I , and C_D). The present implementation of this controller modifies its basic algorithm to incorporate the measured angular velocity, ω , to minimize numerical errors associated with calculating the derivative error, where σ_D is calculated using the difference in this signal from the goal velocity ($\omega_G = \frac{d\theta_G}{dt}$). Each jet is allowed to be set at an initial amplitude-modulation state in the absence of a control signal having the jets operated at the same $\tau_{cycle} = 625\mu s$, and in the presence of a control signal one jet's amplitude is increased, and the opposite jet's amplitude is decreased, effecting a change in the jet activation states. Additionally, the jets relative amplitude are allowed to be scaled by C_I and C_2 coefficients in the controller. External function generators and corresponding amplifiers are used to transform the amplitude-modulation signal into a wave packet for jet operation, where the maximum modulation amplitude corresponds to an output jet momentum coefficient of $C_\mu = 0.003$. This controller executes at $f_{con} = 100Hz$ in the present study, and the depiction of the control scheme is shown in Figure 14.

Determination of the optimal control coefficients (C_D , C_P , and C_I) is found through individual iteration when the model goal is set to the model held steady at the $\theta = 0^\circ$, as shown in Figure 15. To measure the coefficient's efficacy, θ_{RMS} is measured, where the ideal control coefficients produce minimal θ_{RMS} . Initial alteration of these coefficients revealed the control was most sensitive to the C_D coefficient, and that coefficient was varied first in Figure 15a, with $C_P = C_I = 0$. For a negative C_D coefficient, θ_{RMS} increased significantly, and for a positive C_D

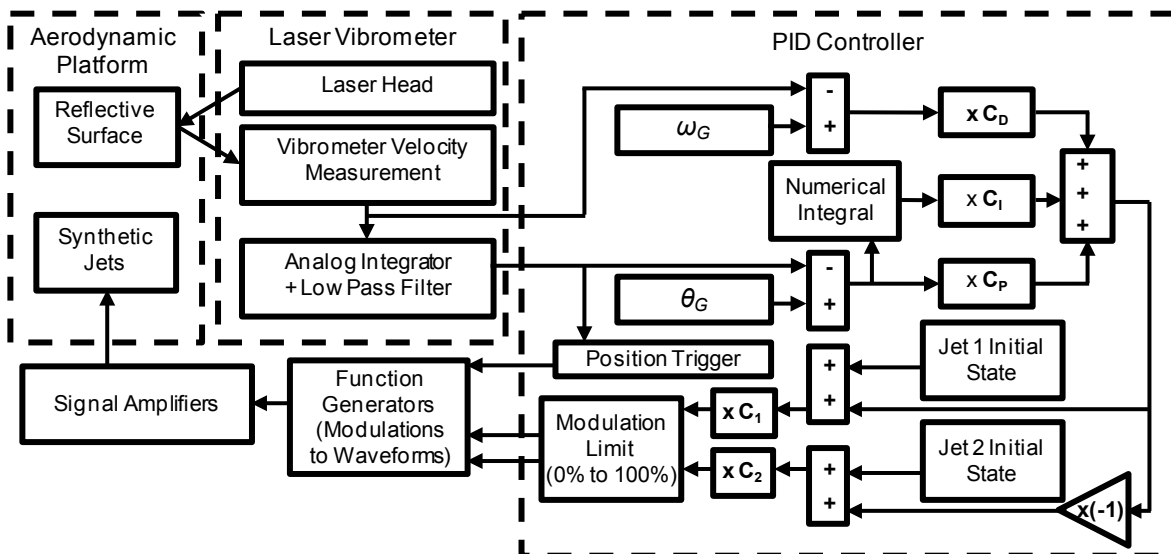


Figure 14: Schematics of the closed-loop PID controller.

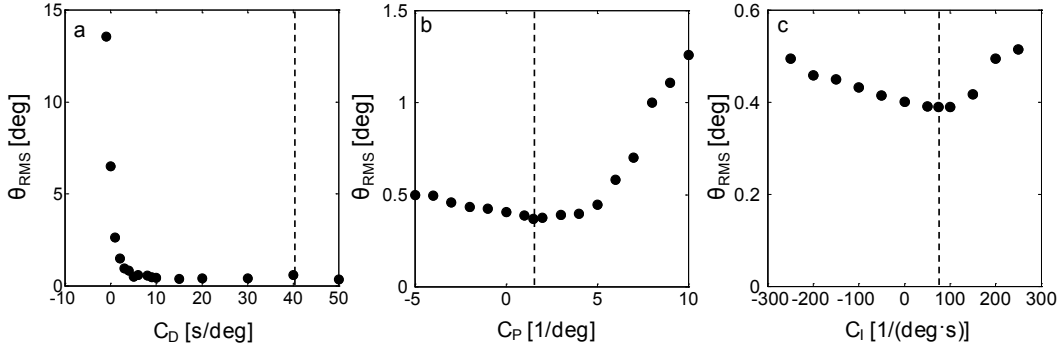


Figure 15: Determination of C_P , C_I , and C_D ($U_0 = 20$ m/s, maximum $C_\mu = 0.003$) for suppression of model oscillations: varied C_D , $C_I=C_P=0$ (a), varied C_P , $C_D = 40$ s/deg, $C_I = 0$ (b), and varied C_I , $C_D = 40$ s/deg, $C_P = 1.5$ /deg (c). Selected operational parameters are shown by dashed lines.

coefficient, θ_{RMS} quickly diminished to an asymptotic value of $\theta_{RMS} = 0.48^\circ$ at $C_D > 10 \frac{s}{deg}$, with the operation C_D chosen to be safely in this region at $C_D = 40 \frac{s}{deg}$. Secondly, the C_P coefficient is varied with this pre-set C_D , and $C_I=0$, as shown in Figure 15b. The variation of θ_{RMS} was much less significant, where the minimized value was found to be $\theta_{RMS} = 0.43^\circ$ at $C_P = 1.5 \frac{1}{deg}$. Finally the C_I coefficient is varied with the chosen C_D and C_P , as shown in Figure 15c. This led to the minimal $\theta_{RMS} = 0.40^\circ$, at $C_I = 75 \frac{1}{deg \cdot s}$, which is used as the operational C_I coefficient.

Three control schemes are singled out as the primary investigations of interest: holding the model steady at $\theta = 0^\circ$, holding the model steady at an offset $\theta > 0^\circ$, and amplification of baseline vibrations. The instantaneous implementation of these control schemes are shown in Figure 16 with a free stream velocity of $U_0 = 20$ m/s during the time span of $600 \tau_{conv}$ uncontrolled, $1200 \tau_{conv}$ controlled, and $600 \tau_{conv}$ uncontrolled. Figure 16a demonstrates the implementation of the controller with a goal $\theta = 0^\circ$, with the controller onset and termination shown with vertical dotted lines, and the desired zero level is also shown as a dotted line for reference. As mentioned above, $\theta_{RMS} = 0.4^\circ$ about zero when implemented. It is important to note that upon the controller onset, the model response reaches its steady state position on the order of $2 \tau_{osc}$, while when terminated, it takes significantly longer to return to its steady state oscillation. As an example of realized offset angle of attack, Figure 16b shows results of implementation of the controller with a goal angle of $\theta = 2^\circ$, with both 0° and 2° shown as referenced dotted lines. This angle positioning was achieved with right jet modulation alone, and this control scheme takes a longer time period to reach a steady state angle, compared to angle of zero degrees (Figure 16a). Figure 16c implements the controller with the coefficients inverted from their optimal values, yielding an amplified response signal of the model vibration, again with zero shown as a reference with a dotted line. Similar to Figure 16a, this control takes around $2 \tau_{osc}$ to reach its controlled state, while needing a significantly longer period of time to return to its free stream vibration, once the control is terminated.

The transient response of each control scheme in Figure 16 is investigated in more detail in Figure 17. Figures 17a-c show the instantaneous time traces corresponding to Figures 16a-c from $120 \tau_{conv}$ prior to $360 \tau_{conv}$ after onset of control. The controller modulation signals are shown to the right jet in Figures 17d-f, and to the left jet in Figures

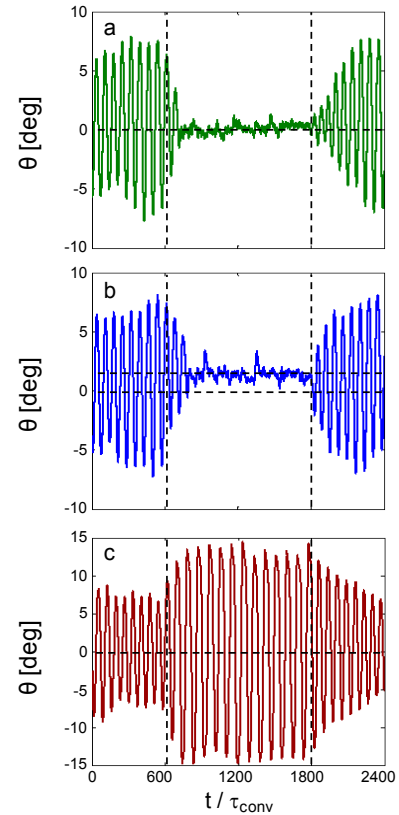


Figure 16: Time-trace of the model deflection angle for the PID closed-loop control ($U_0 = 20$ m/s and maximum $C_\mu = 0.003$) of $\theta = 0^\circ$ (a) and 2° (b) angle of attack, and amplification of oscillations (c).

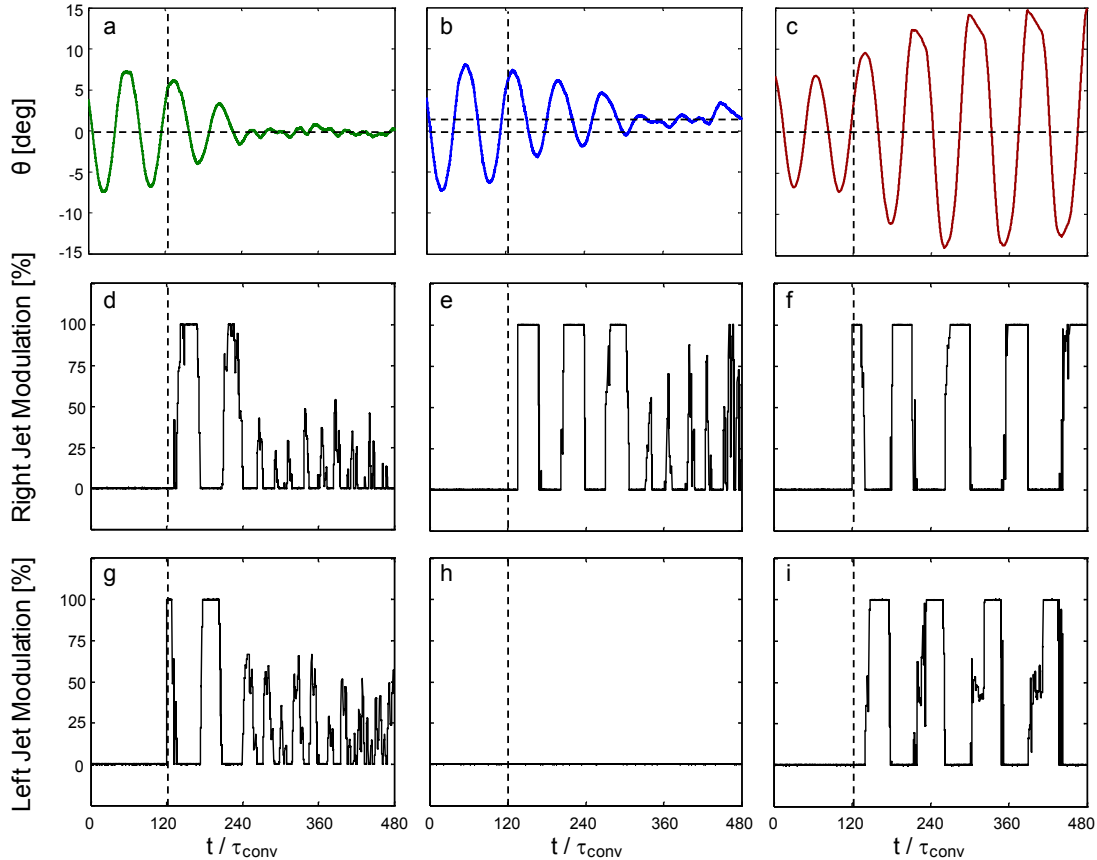


Figure 17: Model deflection (a,b,c) and the corresponding modulation control signals to the right (d,e,f) and left (g,h,i) jet ($U_0 = 20$ m/s and maximum $C_\mu = 0.003$) for $\theta = 0^\circ$ (a,d,g) and 2° (b,e,h) angle of attack, and amplified oscillation amplitude (c,f,i) PID control schemes, with control onset at $t = 120\tau_{conv}$.

17g-i. In Figures 17d and g the jet modulations of amplitude saturate for the first second of activation where the controller is attempting to rapidly compensate from the large differences in desired and measured angle, and settle to rapid minor activations of around 50% of the maximum jet output. Initially, the oscillation is a 1.7 Hz quasi-sinusoidal wave, making the derivative error σ_D a factor of ~ 10 ($2\pi/\tau_{osc}$) times larger than σ_P , which is in turn also ~ 10 times larger than σ_I . The result of this scaling causes the derivative term in the controller to dominate for the first few modulation pulses. This is observed in the first few modulation cycles in Figure 17d, where the right jet initially activates when there is a negative angular velocity, and in the corresponding Figure 17g the left jet activates when there is a positive angular velocity. The resulting activation of the synthetic jets leads to a control that primarily opposes the model's angular velocity. When the model response begins to settle, the other terms in the controller play a larger roll and the modulation signal become smaller, more rapid, and less periodic. Figure 17e is similar to 17d, with the exception that when the model is being held at an offset angle, the right jet modulation has more initial saturated pulses, and the steady angle modulations are larger in magnitude. In Figures 17f and i the model response frequency remains around the same magnitude as the model oscillation frequency before the jet activations were triggered, making σ_D dominate for the entire duration of the controlled response. This causes the model to activate the jets primarily to enhance the model's angular velocity, where the jet modulations do not settle and instead continually saturate for the duration of this control.

The transient response of the controller command $\theta = 0^\circ$, both in activation and termination, is plotted in Figure 18, with this result being the average of 25 data sets. Similar to Figures 6 and 7, the transient response is plotted $120\tau_{conv}$ prior to $600\tau_{conv}$ after the control actuation in Figures 18a and c, and $120\tau_{conv}$ prior to $600\tau_{conv}$ after the control termination in Figures 18b and d, with the control actuation shown in green. Figure 18a shows ω vs. θ , initially forming an ellipsoidal path, where a circular path would represent perfect harmonic motion, and then upon the onset of the jet control, the model forced to $\theta = 0^\circ$ within $2\tau_{osc}$. The observation that the noise on this final model state is smaller than the fluctuation about the instantaneous suppression (Figure 18a) is evidence that the

induced disturbances in the model with the control activated are pseudo random, and average to zero. When the control is terminated in Figure 18b, the model returns to the baseline path at a much slower rate compared to control onset, but at approximately the same rate as open loop actuation (Figure 7b). There is a ringing oscillation present in the center of Figure 18b, showing that the model becomes unstable in this forced position once the control is terminated. Figures 18c and d show M_y vs. θ for the same duration of Figure 18a and b. The onset of the jets in Figure 18c command the model to reach zero angle of attack, but the aerodynamic force is more unstable then the position, leading to the steady state activation to average to a vertical line on this phase plot. Similar to Figure 18b, Figure 18d shows that the termination of the control takes a much larger time period to restore the baseline cycle, where the baseline cycle isn't fully restored even after $600\tau_{conv}$, similar to the open loop control cases in Figures 5 and 6.

A similar study of the transient response of the model is presented for the controller command $\theta = 2^\circ$ in Figure 19, with the control actuation shown in blue. Figures 19a and b show the development of ω vs. θ , and Figures 19c and d show the development of M_y vs. θ . The control onset is shown in Figure 19a and c, where the model is forced to $\theta = 2^\circ$, but a longer time is needed to achieve this goal ($4\tau_{osc}$) due to the controller utilizing one jet as opposed to both to reach its command goal. It is interesting to note that the moment peaks present in the baseline in Figure 19c diminish during the application of control, with large peaks still present in the first τ_{osc} , but these peaks diminish as the range of motion becomes smaller, which is in good agreement with Figures 6 and 7. When the control is established, the location of the model is less steady then when the controller was holding the model at $\theta = 0^\circ$, causing the established position to have a lot more noise in θ , averaging to an ellipse rather than a line (compare Figures 18 and 19). Upon termination of control, in Figures 19b

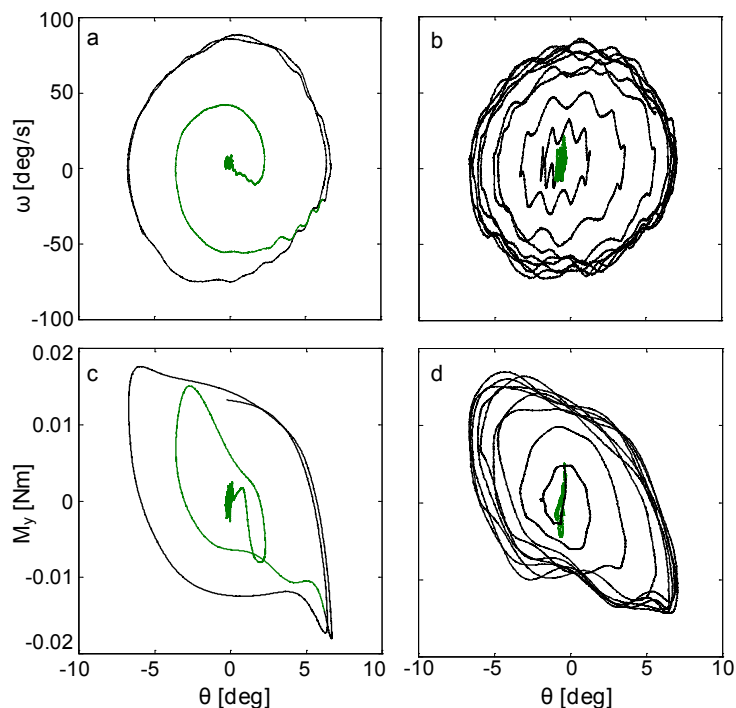


Figure 18. Phase plot of 25 averages of angular velocity, ω (a,b), and yaw moment, M_y (c,d) for $120\tau_{conv}$ prior to $600\tau_{conv}$ after the transient activation (a,c) and termination (b,d) of the $\theta = 0^\circ$ PID control for $U_0 = 20$ m/s and maximum $C_\mu = 0.003$.

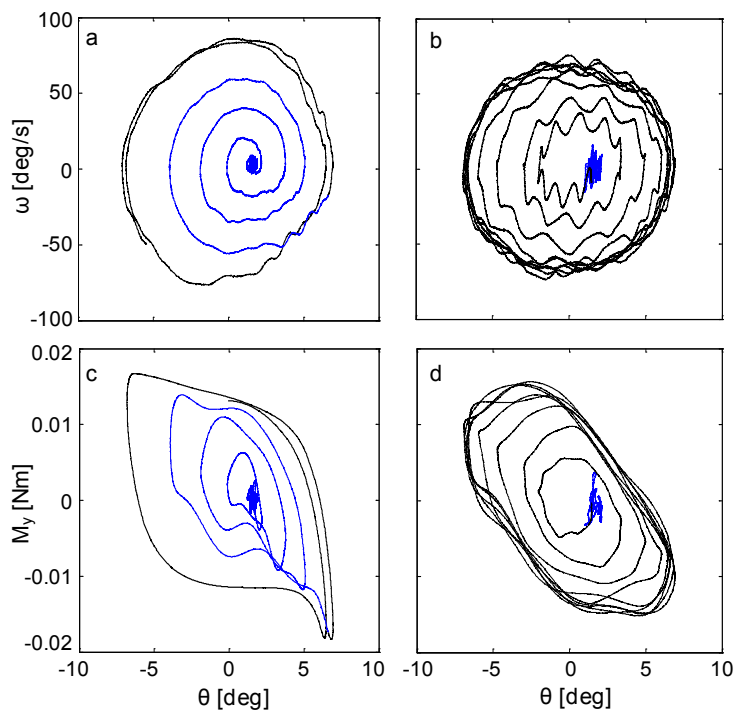


Figure 19. Phase plot of 25 averages of angular velocity, ω (a,b), and yaw moment, M_y (c,d) for $120\tau_{conv}$ prior to $600\tau_{conv}$ after the transient activation(a,c) and termination (b,d) of the $\theta = 2^\circ$ PID control for $U_0 = 20$ m/s and maximum $C_\mu = 0.003$.

and d, the average path has a ringing oscillation, which is a similar instability to that observed in Figures 18b and d, and the termination of the control also requires more than $600\tau_{conv}$ to return to the fully established baseline oscillation.

The amplification closed loop control scheme is investigated in detail in Figure 20, in an analogous fashion to Figures 18 and 19. Upon the presence of actuation in Figures 20a and c the ellipsoidal path is amplified to a new path with the introduction of angular velocity peaks at the extremes of motion, and the moment peaks become much more pronounced. The increase of prominence of the moment peaks with the larger oscillation amplitude shows that the model path is more unstable than it was initially, deviating further from simple harmonic motion, with sudden large aerodynamic moments introduced at the extremes of motion. This effect shows the same trend as Figure 7, where an actuation scheme that decreased the oscillation amplitude also diminished these instabilities. The variation of the path once the control is established is significant, showing a similar development of time scale as the open loop control studies investigated in Figures 6 and 7. Before the termination of control in Figure 20d, the path is significantly different then the path observed 5s after the onset of control in Figure 20c, suggesting that the amplified path is very unstable, and was not fully established in Figure 20c. Upon termination of the amplification control in Figures 20b and d, the model returns to the baseline path at a significantly faster rate than the two held-stationary control schemes, which can be observed by the emergence of the moment peaks in Figure 20d, which were not established in Figures 18d and 19d.

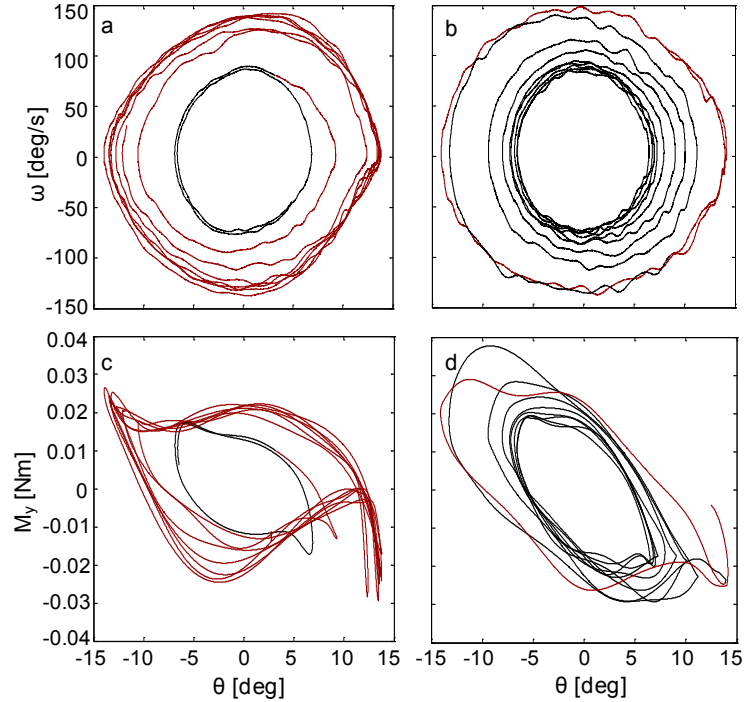


Figure 20. Phase plot of 25 averages of angular velocity, ω (a,b), and yaw moment, M_y (c,d) for $120\tau_{conv}$ prior to $600\tau_{conv}$ after the transient activation (a,c) and termination (b,d) of the amplification PID control for $U_0 = 20$ m/s and maximum $C_\mu = 0.003$.

The effect of the different controller schemes on the model wake is examined using an ensemble average of 2,000 PIV fields shown with streamwise velocity, U , contours in Figures 21a-e, and ζ contours in Figures 21f-j. The

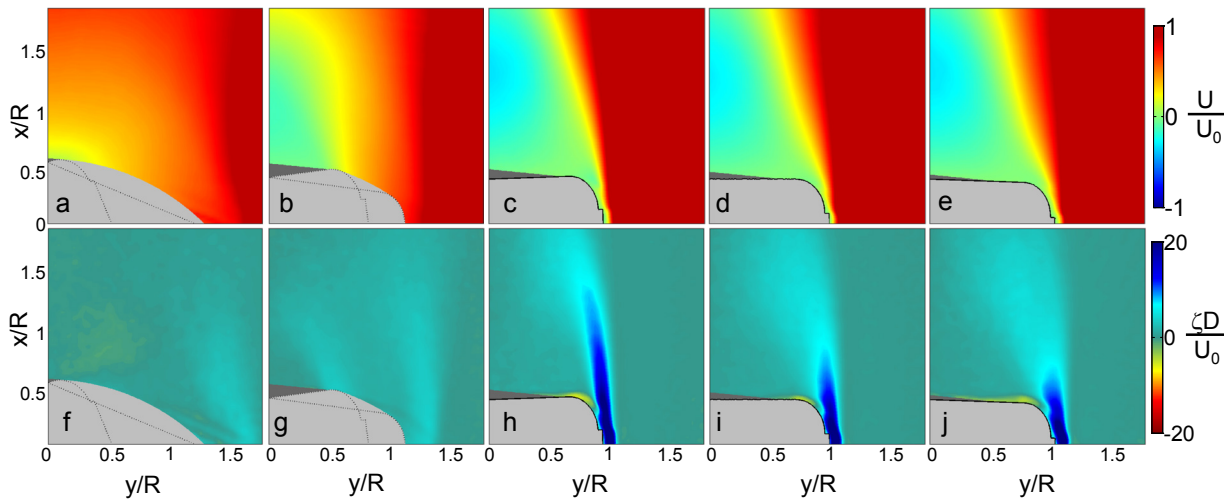


Figure 21: Contour plots of the time-averaged streamwise velocity, U (a-e), and in-plane vorticity, ζ (f-j), for: amplified control (a,f), baseline (b,g), and $\theta = 2^\circ$ (c,h), 0° (d,i), -2° (e,j) control, for $U_0 = 20$ m/s and maximum $C_\mu = 0.003$.

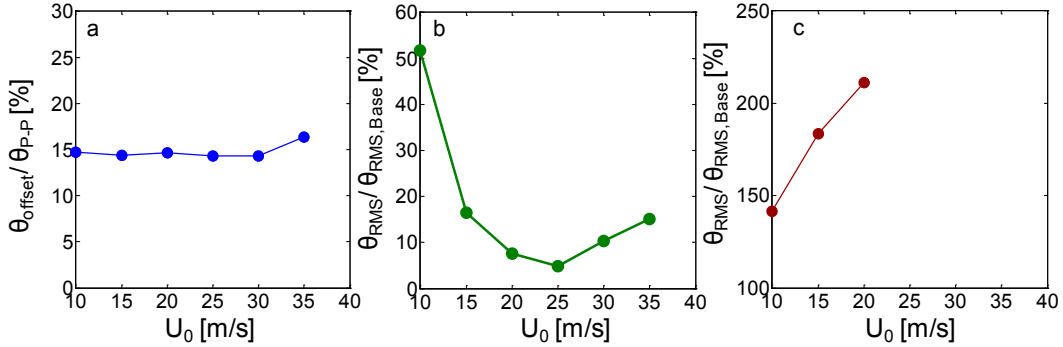


Figure 22: PID control induced steady deflection (a), oscillation suppression (b), and oscillation amplification (c) percentages with the free stream speed, U_0 , at maximum $C_\mu = 0.003$.

biggest average wake disturbance is observed when the controller is set to amplify model's oscillations in Figures 21a and f, with the minimum and maximum range of the model orientation shown with dashed lines at the bottom left of each figure. In this scenario, most of the wake effects are averaged out, with the key note that remnants of the out-of-picture jet are observed with a negative vorticity region when the model is most yawed clockwise, as well as a positive vorticity region which shows remnants of the largest model position when the angular velocity changes sign. Figures 21b and g again average out a lot of the wake's features but give a visual indication of the vorticity shed when the model changes direction at the extremes of its deflection. Figures 21c,d, and e show a developed wake when the model is set to be held steady at $\theta = 2^\circ$, 0° , and -2° , respectively, where even though the model position is different, the wake structure of U is predominantly similar. Figures 21h,i, and j show more clear differences in ζ , where the model being held primarily with the out of plane jet has the largest area of the largest positive vorticity contour, but has the least spread (Figure 21h), and the model being held primarily with the in plane jet has the smallest area of the largest positive vorticity with the most spread (Figure 21j), and the model being held by both jets has an intermediate vorticity contour structure. (Figure 21k).

The results of these three schemes of the controller were analyzed at various wind tunnel speeds, and the results are displayed in Figure 22. Figure 22a shows the ratio of the maximum steady deflection angle obtained, θ_{offset} , normalized by the baseline θ_{P-P} , and plotted against U_0 , where this result appears to be almost invariant at the wind tunnel speeds investigated (10-35m/s). As the baseline vibrations increased approximately linearly with the wind tunnel speed (Figure 3b), the model's steady deflection angle also linearly increased with wind tunnel speed. A reason for this is that the primary force the synthetic jet induces is from vectoring the shear layer, so, as the shear layer becomes faster with U_0 , the induced model force becomes larger as well. Figure 22b displays the θ_{RMS} of the $\theta = 0^\circ$ control compared to θ_{RMS} of the baseline, plotted against U_0 . When U_0 is relatively low, the jets do not effect enough of a force to stabilize the instability force. Also, when U_0 is relatively high, the present C_μ is insufficient to fully vector the wake, which is required to stabilize the model. Therefore, there is a competing control effect, and a maximum reduction of the model oscillations is 95% at $U_0 = 25\text{m/s}$. Figure 22c displays the θ_{RMS} of the amplification control compared to θ_{RMS} of the baseline, plotted against U_0 . The maximum amplification percentage is shown for $U_0 = 10, 15, \text{ and } 20$ m/s, where higher U_0 had excited the oscillation angles outside of the vibrometer range ($\sim \pm 15^\circ$), and therefore could not be recorded.

VII. Conclusions

A single degree of freedom support system of an axisymmetric wind tunnel model was designed and built to enable 'free' model dynamic motion in yaw, in the absence and presence of aerodynamic flow control. The model is supported by a vertical thin steel wire that passes through the model, and is secured such that there is minimal friction, translational and rotational vibrations. The model is also equipped with two aft independently-driven synthetic jet actuators that are centered about the plane of the model yawing motion. Motion is characterized using a laser vibrometer aligned with the yaw plane, and planar PIV measurements are utilized to characterize the coupled aft flow dynamics, including the near-wake topology. It is found that, in the absence of actuation, the interaction of the cross flow with the model leads to natural time-periodic yaw oscillations which are attributed to a phase lag between the wake responses (and in turn force/moment response) and the dynamic body orientation. The predominant oscillation frequency and the oscillation amplitude are both directly proportional to the free stream speed.

Open-loop continuous actuation with either one or both control jets demonstrated that such a control scheme can be applied to either suppress natural oscillations of the model by up to about 60%, or to shift the center of the body oscillations, along with suppression in amplitude. Open-loop actuation was used to characterize the time scale at which the full actuation effect is established, and it is found that the transient effects of the actuation onset die out in less than 1.5 convective time scales. Transient coupling between the jet actuation onset and the flow/wake response also revealed that the dominant vectoring effect can be attributed to the train of small-scale vortical structures that are formed at the jet orifice, which dominate the effect of a large-scale starting vortex that is advected into the near wake.

To fully exploit the capabilities of active flow control to steer the attitude of the dynamically yawing model, a PID closed-loop control is developed and utilized to control a desired trajectory. The model's measured displacement is used as the control input, while the amplitude modulation of both of the jets prescribed outputs at the fixed actuation frequency is the control output. The present experiments demonstrated that this closed-loop control is capable of dramatically suppressing the model's unstable yaw oscillations, in excess of 90% in some instances. Furthermore, in reversed operation, the same control scheme can dramatically amplify natural oscillation, more than 200% of the natural amplitude. Finally, closed-loop control can deflect the body relative to the free stream and maintain a steady nonzero angle of attack within a range of 15% of the natural oscillation extent.

Acknowledgment

This work has been supported by the Army Research Office monitored by Dr. Frederick Ferguson.

References

- ¹Hsiao, F. B., Liu, C. F., and Shyu, J. Y., "Control of Wall-Separated Flow by Internal Acoustic Excitation", *AIAA J.*, Vol. 28, 1990, pp. 1440-1446.
- ²Williams, D., Acharya, M., Bernhardt, K. & Yang, P., "The Mechanism of Flow Control on a Cylinder with the Unsteady Bleed Technique", *AIAA Paper 1991-0039*, 1991.
- ³Chang, R. C., Hsiao, F. B., and Shyu, R. N., "Forcing Level Effects of Internal Acoustic Excitation on the Improvement of Airfoil Performance", *J. Aircraft*, Vol. 29, 1992, pp. 823-829.
- ⁴Seifert, A., Bachar, T., Koss, D., Shepshelovich, M. and Wagnanski, I., "Oscillatory Blowing: A Tool to Delay Boundary-Layer Separation", *AIAA J.*, Vol. 31, 1993, pp. 2052-2060.
- ⁵Erk, P. P., "Separation Control on a Post-stall Airfoil using Acoustically Generated Perturbations", PhD Thesis, Tech. Univ. Berlin, Germany, 1997.
- ⁶Smith, D. R., Amitay, M., Kibens, V., Parekh, D., and Glezer, A., "Modification of Lifting Body Aerodynamics Using Synthetic Jet Actuators", *AIAA Paper 1998-0209*, 1998.
- ⁷Amitay, M., Smith, D. R., Kibens, V., Parekh, D. E., and Glezer, A., "Aerodynamic Flow Control over an Unconventional Airfoil Using Synthetic Jet Actuators", *AIAA J.*, Vol. 39, 2001, pp. 361-370.
- ⁸Honohan, A. M., Amitay, M., and Glezer, A., "Aerodynamic Control using Synthetic Jets", *AIAA Paper 2000-2401*, 2000.
- ⁹Newman, B.G., "The Deflexion of Plane Jets by Adjacent Boundaries-Coanda Effect", *Boundary Layer and Flow Control Principles and Applications*, Vol. 1, 1961, pp. 232-264.
- ¹⁰Nagib, H. M., Reisenthel, P. H., and Koga, D. J. "On the Dynamical Scaling of Forced Unsteady Flows", *AIAA Paper 1985-0553*, 1985.
- ¹¹Lo, K. P., Elkins, C. J., Eaton, J. K., "Separation Control in a Conical Diffuser with an Annular Inlet: Center Body Wake Separation", *Exp. Fluids*, Vol 53, 2012, pp 1317-1326.
- ¹²Freund, J. B., Mungal, M. G., "Drag and Wake Modification of Axisymmetric Bluff Bodies Using Coanda Blowing", *J. Aircraft*, Vol. 31, 1994, pp. 572-578
- ¹³Sigurdson, L. W., "The Structure and Control of a Turbulent Reattaching Flow", *J. Fluid Mech.*, Vol. 298, 1995, pp. 139-165.
- ¹⁴Rinehart, C., McMichael, J. M., and Glezer, A., "Transitory Flow and Force Development on a Body of Revolution Using Synthetic Jet Actuation", *AIAA Paper 2003-0618*, 2003.
- ¹⁵Rinehart, C., "Aerodynamic Forces Induced by Controlled Transitory Flow on a Body of Revolution", Ph. D. Thesis, Georgia Institute of Technology, 2011.
- ¹⁶McMichael, J., Lovas, A., Plostins, P., Sahu J., Brown, G., and Glezer, A., "Microadaptive Flow Control Applied to a Spinning Projectile", *AIAA Paper 2004-2512*, 2004.
- ¹⁷Abramson, P., Vukasinovic, B., and Glezer, A., "Direct Measurements of Controlled Aerodynamic Forces on a Wire-suspended Axisymmetric Body", *Exp. Fluids*, Vol. 50, 2011, pp. 1711-1725.
- ¹⁸Corke, T. C., Tillotson, D., Patel, M. P., Su, W. J., Toldeo, W., "Radius Flow Vectoring for Projectile Drag and Steering Control Using Plasma Actuators", *AIAA Paper 2008-3769*, 2008.
- ¹⁹Abramson, P., Vukasinovic, B., and Glezer, A., Fluidic Control of Aerodynamic Forces on a Bluff Body of Revolution, *AIAA J.*, Vol. 50, pp.832-843, 2012.

²⁰Lambert, T. J., Vukasinovic, B., and Glezer, A. "Unsteady Aerodynamic Flow Control of a Wire-Suspended, Moving Axisymmetric Body", *AIAA Paper* 2012-0073, 2012.

²¹Higuchi, H., Van Langen, P., Sawada, H., Timney, C. E., "Axial Flow Over a Blunt Circular Cylinder With and Without Shear Layer Reattachment", *J. Fluids Struct.*, Vol. 22, 1996, pp. 949-959.

²²Kutay, A. T., Calise, A. J., Muse, J. A., "A 1-DOF Wind Tunnel Experiment in Adaptive Flow Control", *AIAA Paper* 2006-6430, 2003.